



Speed function effects on properties of Ti-5Al-5Mo-5V-1Cr-1Fe alloy manufactured by electron beam melting

Marcin Madeja¹ · Robert Dziejdzic¹

Received: 6 June 2023 / Accepted: 22 August 2023 / Published online: 4 September 2023
© The Author(s) 2023

Abstract

The speed function (SF) parameter, which is a unique combination of beam speed and beam current, is one of the most important parameters of the electron beam melting (PBF-EB) production process. It allows the same process conditions (size of the melt pool, process temperature, etc.) to be maintained for parts with different geometries and sizes. The aim of this research was to understand the effect of SF on the Ti-5Al-5Mo-5V-1Cr-1Fe alloy produced by electron beam melting technology. The results showed that increasing the SF from 86 to 116 resulted in a decrease in the average process temperature, a decrease in the length of the α phase plates, and change in the proportion of α and β phases from 53% (SF 86) to 50% (SF 116) of the β phases. Differences in microstructure (column diameters, thickness, and length of α -phase plates), phase composition, microhardness, porosity at the bottom, and top of the samples were observed on all samples. The mechanical property analysis did not show a significant effect of SF on elongation, but an increase in SF from 86 to 96 resulted in an increase in ultimate tensile strength (UTS) of approximately 7%, whilst an additional increase to 116 resulted in a decrease in UTS of approximately 8.5% compared to SF 96. From the results, it can be seen that the microstructural and mechanical properties of the material strongly depend on the SF. Based on it, SF 86 can be considered as the recommended value for the manufacture of Ti-55511 alloy parts.

Keywords Electron beam melting · PBF-EB · Speed function · Ti-55511 · Ti-5Al-5Mo-5V-1Cr-1Fe titanium alloy

1 Introduction

Titanium and its alloys are widely used in the aerospace sector due to their combination of high specific strength (strength-to-weight ratio), which remains effective even at elevated temperatures, along with their crack resistance and high corrosion resistance. Moreover, their use is increasingly being considered in industrial and commercial applications, including oil refining, chemical processing, medical implants, pollution control, nuclear waste storage, food processing, electrochemical applications, and marine applications, amongst others. Titanium alloys can be classified based on their microstructure at room temperature as α , near α , $\alpha + \beta$, near β , or stable β . Alloying elements for titanium

can be divided into three classes: (1) α -stabilisers, including Al, O, N and C; (2) β -stabilisers, such as Mo, V, Nb, Ta (isomorphous), Fe, W, Cr, Si, Co, Mn, and H (eutectoid); and (3) neutrals, represented by Zr. Whilst α and nearly α titanium alloys have excellent corrosion resistance, they show limited strength at low temperatures. In contrast, $\alpha + \beta$ alloys achieve greater strength due to the presence of both α and β phases. The properties of these materials depend on factors such as composition, proportions of α and β phases, heat treatment, and thermomechanical processing conditions [1–5].

Near- β titanium alloys belong to a group of alloys with a microstructure consisting of α and β phases. They are commonly used in the aerospace and chemical industries because of their high corrosion resistance ($E_{\text{corr}} - 300/-800$ mV (SCE)) [6–9] and relative strength ($320 \text{ MPa cm}^3 \text{ g}^{-1}$) [10, 11]. This alloy category includes, amongst others (Ti-10V-2Fe-3Al, Ti-5.8Al-4Sn-3.5Zr-0.7Nb-0.5Mo-0.35Si, Ti-5Al-2.5Sn, and Ti-5Al-5V-5Mo-3Cr), the alloy Ti-5Al-5Mo-5V-1Cr-1Fe (Ti-55511), also designated as VT22. It is characterised by its ability to operate short-term at temperatures of 750–800 °C, high strength (1080–1280 MPa), and

✉ Marcin Madeja
Marcin.Madeja@pwr.edu.pl
Robert Dziejdzic
robert.dziejdzic@pwr.edu.pl

¹ Faculty of Mechanical Engineering, Wrocław University of Science and Technology, 50-370 Wrocław, Poland

high fracture toughness ($66\text{--}77\text{ MPa}\cdot\text{m}^{0.5}$) [12–14]. It can be heat treated and thermomechanically treated, thus affecting fatigue properties, tensile strength, and ductility [12, 15, 16] by obtaining a microstructure with a bimodal grain shape, an equiaxial grain shape, or the Widmanstätten structure with a lamellar grain shape [13, 14, 17]. In industry, the alloy is used for parts subjected to high mechanical stress, such as low-pressure compressor blade components, chassis components, and parts of the fuel system [18]. The conventional way of manufacturing parts from Ti-55511 alloy is by hot forming, thermo-mechanical machining, or casting. Shaping of parts manufactured from Ti-55511 alloy is usually carried out by machining, forging, or injection casting processes. These processes generate high costs and are time-consuming to implement [19–23].

Parts manufactured from Ti-55511 alloy are produced mainly as units (chassis components) or small batch production (fuel system parts). For these types of production, it is possible to reduce the total cost and manufacturing time by using powder-bed-fusion (PBF) additive manufacturing (AM) technologies such as laser powder-bed fusion (PBF-LB) or electron beam melting (PBF-EB). PBF technologies allow multiple components to be manufactured as a single part or parts with complex geometries. This significantly reduces production times [24, 25]. Parts manufactured using PBF typically have comparable or superior mechanical properties compared to components manufactured using traditional manufacturing methods [26]. The implementation of a new material in PBF technology is associated with the need to develop technological parameters to obtain specific mechanical properties, microstructure, and elimination of undesirable discontinuities, e.g., porosity. In PBF technologies (PBF-LB, PBF-EB), the key to a stable process allowing specific properties to be obtained is to maintain an equal-sized and stable melt pool and to supply the appropriate amount of energy. This is realised by appropriately controlling the process parameters, setting the laser/electron beam power, its speed, hatching strategy, etc. At constant power, changing the speed significantly affects the amount of energy delivered, thus the solidification process of the material and mechanical properties [27–30]. If the beam speed is too low, too much energy is delivered, leading to over melting, vapourisation of some elements of the alloy, and the formation of a molten metal pool with different surface tensions due to temperature gradients, causing Marangoni convection, turbulence and keyhole phenomenon. Rapid cooling of the molten metal pool leads to the entrapping of gas bubbles that could escape from the melt pool before solidification results in the occurrence of gas porosity [31–33]. For the medium speed range, the “right” amount of energy is supplied to the process. This allows for the reduction or elimination of discontinuities, obtaining a certain microstructure, properties, etc. At a too high speed, the energy supplied is

insufficient, resulting in discontinuities or lack of melting of the material and consequently poor mechanical properties.

The selection of parameters in PBF processes to achieve the desired microstructure, porosity, etc. is usually done on the basis of the production of small cuboidal samples in “manual mode” where users can set and control all values of process. Also process parameters are fixed throughout the manufacturing process. The use of selected parameters for larger parts usually involves additional testing or separate studies. This is due to changes in energy delivery, energy accumulation, heat dissipation rate, etc. [34].

To eliminate the need to adapt the parameters each time to the part being produced, Arcam AB (Arcam EBM, Ge), the developer of PBF-EB technology, has developed a control algorithm that, based on the cross-sectional area of the part being produced, adjusts the speed and power of the beam to achieve constant process conditions [34]. One of the functions of the control algorithm is the so-called speed function (SF). It is a unitless value in the range from 1 to 150; a higher value corresponds with higher beam speed. Each value of SF is a unique set of beam speeds and beam current [35–37]. The control algorithm for a given value of SF and beam current reads the value of beam speed from a table; this allows to maintain an equal-sized and stable melt pool [34]. This algorithm in “automatic mode” controls and altered process parameters, allowing to produce various part, different sizes, and shapes, with theoretical same conditions every time (melt pool size, surface temperature) [38–41]. For melting given part of the cross-section, for given value of speed function, the algorithm first calculates beam current, then from speed function table reads beam speed. This procedure is applied for each layer. If the value of SF is too low, energy input for the given cross-section will be too high and may cause e.g. over melting. If it will be too high energy will be insufficient to fully melt given cross section and result in e.g. high porosity. Cunningham et al. [36] and Gong et al. 2014a [37] have shown from experimental studies that for a fixed value of beam current, an increase in SF results in a decrease in the size of the melt pool. To maintain the size of the melt pool set by SF for a given beam current, it is necessary to increase the beam speed. Increasing the beam speed without changing the beam current affects the energy supplied to the material [41, 42]. This translates directly into the occurrence of discontinuities in the material produced. In the Ti-6Al-4V alloy produced by PBF-EB, there is a strong correlation between the SF value and porosity. An increase in SF from a value of 60 to 180 increases the number of discontinuities from about 0.5% (SF 60) to about 5% for SF 180. A higher SF increases porosity by creating entrapped, unmelted powder particles [36, 39]. Unocic et al. [40] in their study of parameter selection for the Haynes 282 nickel alloy noted that SF in the range 55–75 influences the occurrence of discontinuities, as in the case of Ti-6Al-4V,

with an increase in SF not always resulting in an increase in porosity. For SF 65, they obtained the lowest value of 0.17%.

In addition to affecting material continuity, SF also affects microstructure. Cheng et al. [41] and Wang et al. 2018a [43] in similar studies analysed the effect of process parameters on the thermal characteristics of Ti-6Al-4V in PBF-EB. They showed that increasing the SF from 20 to 50 and thus the beam speed, the cooling rate and the thermal gradient result in the formation of smaller columnar β grains and the increase of α' phase. According to Hall–Petch’s relations, a finer microstructure increases material mechanical properties, for Ti-6Al-4V an increase in SF from 20 to 50 increases the value of Young’s modulus by approximately 10%, in the case of hardness the change can range from approximately 5% [43] to 25% [44]. Wang et al. 2018b [45] in a study on the selection of PBF-EB process parameters for 316L steel showed that an increase in SF increases the porosity of the samples, whilst it does not affect the fineness of the microstructure. He also showed that increasing the SF from 150 to 170 causes a decrease in strength and an increase in elongation of about 11% and 15%, respectively.

The aim of the research presented in this article is to determine the effect of the values of the speed function on the properties of near- β titanium alloy (Ti-5Al-5Mo-5V-1Cr-1Fe) produced by PBF-EB. By understanding the effect of SF on material characteristics, it will be possible to predict properties for parts with complex geometries.

2 Materials and method

The alloy used for this study was Ti-55511 in powder form produced using Atmospheric Plasma Spray (APS) technology (Fig. 1a), which was characterised by almost perfectly spherical particles.

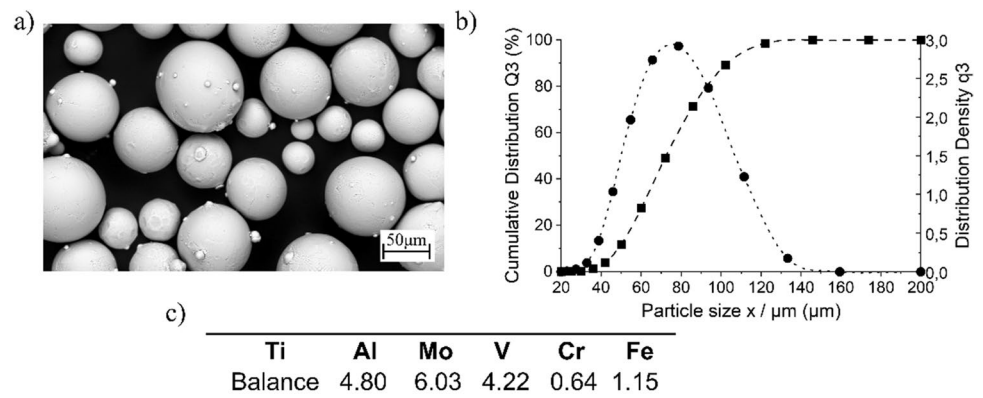
The particle size of the powder was determined by laser diffraction (Fig. 1b); the cumulative distribution Q3 (volume-base diameter) was determined by dynamic image analysis, in accordance with ISO 13320:2009. The obtained

powder distribution sizes for D10.3, D50.3 and D90.3 were $49.18 \pm 0.026 \mu\text{m}$, $77.56 \pm 0.131 \mu\text{m}$, and $108.95 \pm 0.112 \mu\text{m}$, respectively.

In Fig. 1c, the chemical composition of the powder made from the Ti-55511 alloy is presented in the as-delivery condition. Compared to the standard alloy composition according to GOST 19807: 1991 (wt%, Al 4.4–5.7%, Mo 4.0–5.5%, V 4.0–5.5%, Cr 0.5–1.5%, Fe 0.5–1.5%), it can be seen that the values of the main alloy elements in the examined powder were within the standard, with the exception of molybdenum, whose content exceeded the maximum value by approximately 0.8%. The increased molybdenum content in the powder is favourable because of the high tendency of this element to evaporate.

Cylindrical samples, in orientation perpendicular to the work platform, with a diameter of 10 mm and a height of 75 mm were fabricated on an EBM Arcam A1 with 3.2 SP3 (ARCAM AB, Mölndal, Sweden) using “automatic mode.” Sixteen samples for given SF, in separate processes, were made. Three values of SF were chosen 86–96–116. SF 96 represent a set of parameters that had been studied in previous work [31]: current 9.5 mA, scanning speed 3800, and energy 30 J mm^{-3} . SF 86 an SF 116 were chosen to evaluate influence of speed and volume energy. Other process parameters were as follows: layer thickness $50 \mu\text{m}$, snake-like (zig-zag) hatching strategy with a line offset of $100 \mu\text{m}$, average cathode current 9.5 mA (min 4.5 mA, max 13.5 mA), average beam speed in the range $3400\text{--}3800\text{--}4400 \text{ mm s}^{-1}$, average volume energy $34\text{--}30\text{--}26 \text{ J mm}^{-3}$ (SF 86, SF 96, and SF 116, respectively), process start temperature 730°C , and working pressure $2 \times 10^{-3} \text{ mbar}$. The microstructure of the samples was observed on the surface parallel to the fabrication direction. In order to reveal it, the samples were mechanically ground with sandpapers, polished on an OPS solution, and then washed with ethanol. The polished samples were etched with Kroll’s reagent (2% HF, 5% HNO_3 , and 93% H_2O). The microstructures of the samples were observed with a scanning electron microscope and optical microscope.

Fig. 1 Powder used in the study. **a)** SEM (BSE) image of powder and **b)** analysis of the size distribution of the Ti-55511 powder fractions; dotted line—cumulative distribution; dashed line—distribution density; **c)** chemical composition (%wt) of Ti-55511 alloy used in studies [46]



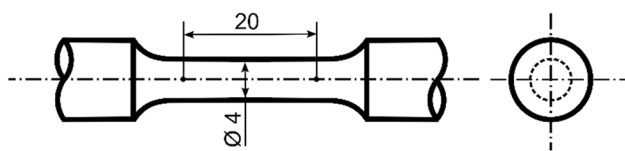


Fig. 2 Geometry of the specimens for the tensile test (ASTM E8/E8M)

Hardness was measured on the surface parallel to the manufacturing direction using the Vickers HV1 method (Zwick-Roell ZHV μ -A hardness tester) in accordance with ISO EN ISO 6507. The mean value for the measurement was obtained by making 12 indentations on an area of 5 \times 5 mm. All measurements, i.e. microstructure, phase composition, and hardness, were measured at approximately 5 mm from the bottom (referred to as B or bottom) and top of the sample (referred to as T or top).

The static tensile test was carried out according to ISO 6892 on an INSTRON 3384 testing machine. The measurement was carried out at a strain rate of 2 mm/min. Samples with a geometry consistent with ASTM E8/E8M-22 were used, with a gauge section diameter of 4 mm and a gauge section length of 20 mm (Fig. 2). The sample shape, dimensions, and surface quality were obtained by machining.

A 150 kN load cell and a noncontact videoextensometer (AVE 2663–821) were used in the tests. The dependence of the tensile force on the increase in sample length was recorded during the test. As a result of the tests, the following were determined: ultimate tensile strength (UTS) [MPa], conventional yield strength (YS) [MPa], and strain ϵ [%]. Porosity of PBF-EB fabricated samples was measured at the height 5 mm from bottom and top in the vertical cross-sections, for each of three, randomly selected, samples for each value of SF. Images of size 7 \times 7 mm, were taken with a confocal microscope (Olympus LEXT 4000). Image analysis was done using ImageJ software, which calculated by the means of the area ratio of pores and total area of micrographs. Calculated area fraction was regarded as porosity. Microstructure observations were performed using a ZEISS EVO 25 scanning electron microscope. Images were taken using a BSE detector at an accelerating voltage of 20 kV. Phase composition analysis was carried out on a surface parallel to the fabrication direction, using a Rigaku model MiniFlex 600 X-ray diffractometer equipped with a HyPix strip detector. Phase measurements were carried out over an angular range of 2θ from 30° to 90° using a 1.5 kW copper lamp. The angular velocity during the measurements was 4°/min. To determine the phase composition, we used Rietveld analysis. The chemical composition was determined on non-etched metallographic samples using an Energy Dispersive X-ray Fluorescence Spectro XEPOS spectrometer.

3 Results and discussion

3.1 Chemical composition

Analysis of the chemical composition of the samples after the PBF-EB process showed that the content of alloy elements changed regardless of the SF value used (Fig. 3).

A decrease in the content of alloy elements was observed, in relation to the initial composition determined for the powder, for molybdenum, vanadium, and iron, with only the vanadium content falling below that determined by the standard for the alloy under study. The largest decrease from the initial chemical composition was recorded for molybdenum from 6% to 4.1% for SF 86. In addition to the decrease in elemental content, an increase in the amount of chromium and aluminium was also registered. In the case of chromium, this was an increase from 0.64% to 0.89%. For aluminium, the change in content was the greatest, increasing from 4.8% to 5.71% for SF 96 and 5.95% for SF 86.

3.2 Phase composition

The phase analysis carried out on samples with different SF showed the presence of two main phases characteristic of this alloy: α and β phase (Fig. 4).

Depending on the SF value used, the intensity of the peaks with respect to the crystallographic planes varies. The largest differences were observed for phase β in orientations (110) and (200) and for phase α in orientation (101). In the remaining cases, the intensity of the peaks was similar regardless of the SF value. When the XRD patterns for the powder before and after the process and for the fabricated samples are compared, it can be seen that the same changes in phase composition occur in the powder as in the fabricated samples. The intensity of the peaks is lower due to the

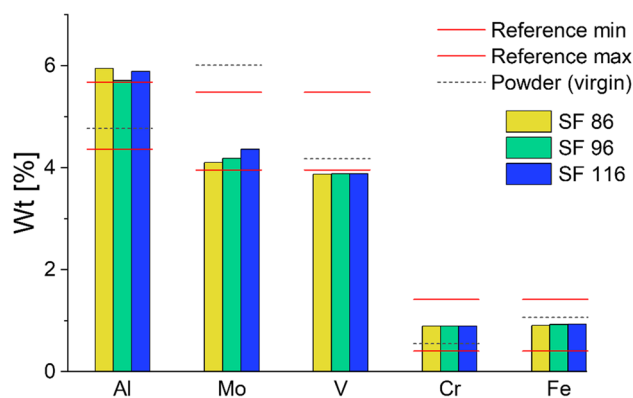


Fig. 3 Comparison of the chemical composition of samples after the PBF-EB process for different SF values. Reference values (min, max) according to GOST 19807: 1991 [47]

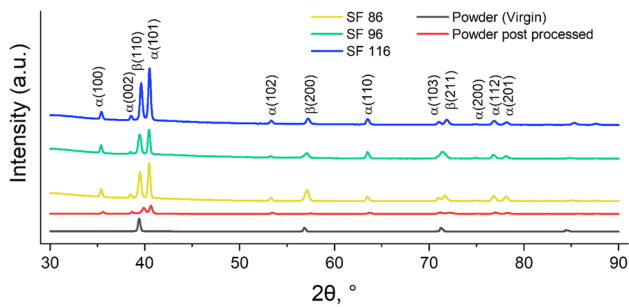


Fig. 4 The XRD (X-ray diffraction) patterns for Ti-55511 samples after the PBF-EB process with SF 86, SF 98, and SF 116 and for the new powder and the powder used in the PBF-EB process

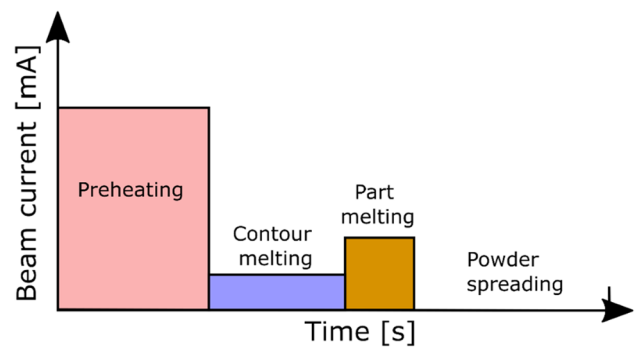


Fig. 6 Schematic representation of layer processing in the PBF-EB process

lack of a transition from solid to liquid and back to solid as is the case for the fabricated samples.

By comparing the phase contribution depending on SF (Fig. 5) and the measurement location (top and bottom), it can be seen that for SF 86, the α -phase content is higher in the bottom part of the sample compared to the upper part. In the case of SF 96, the reverse dependence occurs, with the α -phase content in the bottom part being lower than that in the upper part. For SF 116, the phase contribution in the top and bottom part of the samples is similar.

The layer processing in PBF-EB is divided into four stages: powder heating, contour melting, material melting, and application of a new powder layer (powder spreading) [48, 49] (Fig. 6). Depending on the process parameters for each stage, the amount of energy supplied varies.

Based on the information collected during the process and the experimental measurements, the cathode current and the beam speed were determined for each stage (Fig. 6). On this basis, the total volumetric energy (E_v) supplied to the process was calculated as a function of the SF value. The calculation was based on Eq. (1).

$$E_v = \frac{U \cdot I}{V \cdot l_t \cdot l_o} \left[\frac{J}{mm^3} \right] \tag{1}$$

where U is accelerating voltage [V], I is cathode current [mA], V is scanning speed [$mm\ s^{-1}$], l_t is layer thickness [mm], and l_o is line offset [mm].

For SF 86 E_v was $330\ J\ mm^{-3}$, $329\ J\ mm^{-3}$ for SF 96, and $326\ J\ mm^{-3}$ for SF 116. It can be seen that the differences between the results do not exceed 1%. Such a small difference should not affect the results so significantly.

In the tests carried out, the process parameters (speed and cathode currents) for the different stages of the layer processing, with the exception of the part-melting stage, were the same. This is due to the fact that the cross-section of the melted layer for all SF values was the same. The only variable was the speed of the beam movement, which is related to the SF value. For constant process parameters for preheat and contour, the total energy is about $299\ J\ mm^{-3}$, which is approximately 90% of the energy delivered to each layer. This means that the energy supplied to the process in these two stages is sufficient to maintain the elevated process temperature [48, 50] taking into account the losses due to convection and radiation. For titanium alloys, the recommended process temperature is in the range of approximately $700^\circ C - 800^\circ C$ [34], which corresponds to an approximately 0.4–0.5 of melting point. Depending on the energy supplied in the part melting stage, the process temperature can be closer to the lower or higher range. For SF 86 the volumetric energy delivered to the melted section was $34\ J\ mm^{-3}$, for SF 96 $30\ J\ mm^{-3}$, and for SF 116 $26\ J\ mm^{-3}$. It can therefore be assumed that for SF 86 samples, the temperature in and around the samples during the process should be the highest of the SF values analysed. The phase composition results obtained (Fig. 5) and the temperature readings of the phase transformation curve (Fig. 7) indicate it.

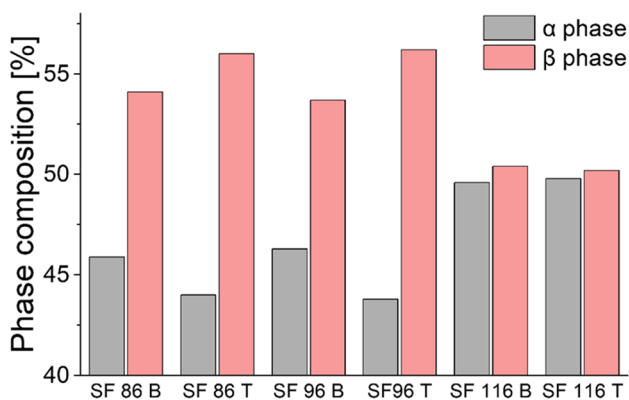


Fig. 5 Comparison of XRD results of individual phases in samples produced with different SF values. B: bottom; T: top. The values were calculated using the Rietveld method

This indicated that, over time, the amount of energy supplied was slightly higher than the losses and thus the process temperature was lower than the initial

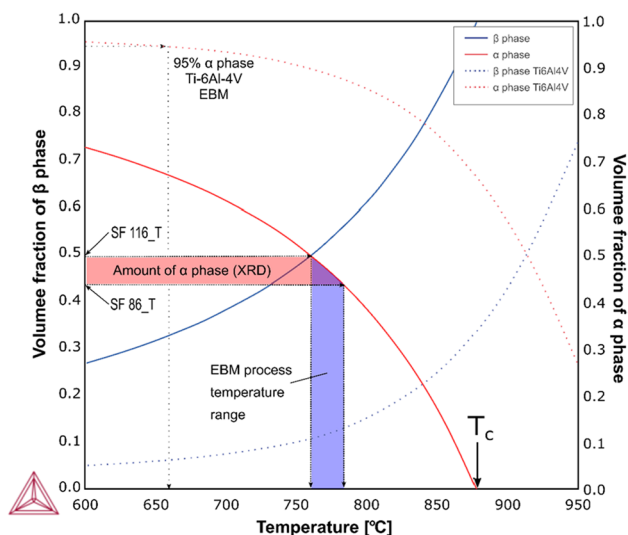


Fig. 7 Phase transformation curves for the alloy used in the study

Table 1 Comparison of estimated process temperature (°C) determined from the phase composition

	SF 86	SF 96	SF 116
Bottom	779	775	754
Top	783	766	753
Average	781	770.5	753.5

temperature. For SF 116, the amount of energy supplied was sufficient to mitigate the losses due to convection and radiation and to maintain a temperature allowing a 50% contribution of the main phases (α , β), throughout the process. The result for SF 116 was an $\alpha + \beta$ structure with a 50% contribution of the individual phases.

Based on the chemical composition of the samples produced with different values of SF (Fig. 3), the temperature-dependent phase transformation curves were determined using Thermo-Calc software (Fig. 7). With the knowledge of the phase composition and temperature-dependent phase transformation curves, we determined the process temperatures for the top and bottom parts of the samples. The results are summarised in Table 1.

Although the Ti-55511 alloy is a near β -type alloy, due to the high process temperature, the α -phase content will be higher than for conventional fabrication or for the PBF-EB-produced Ti-6Al-4V alloy. This is a direct result of the fact that the PBF-EB process temperature for Ti-55511 is much closer to the β -transus temperature than for Ti-6Al-4V, as shown in Fig. 7.

3.3 Microstructure

A characteristic feature of PBF technology that includes PBF-EB is the appearance of columnar grains which are formed by epitaxial growth resulting from high temperature gradients, solidification rates [51–53]. In the case of titanium alloys, Inconel, etc., with cells having a cubic crystal structure (face centred cubic (FCC) or body centred cubic (BCC)), the direction of grain growth, with epitaxial growth, is along one of its crystallographic orientations which forms the smallest angle with the local temperature gradient [54, 55]. In the case of PBF, the temperature gradient is usually directed parallel to the build direction. In PBF-EB processed Ti-6Al-4V alloy strong texture in building direction (001) phase was found (for β phase) by Formanoir et al. [56]. The α phase texture was weaker than high temperature β phase. As authors stated this was a result of the Burgers relationship, up to 12 crystallographic α variants can indeed form in each β grain during the β - α transformation, resulting in a substantial decrease in texture intensity. In their work, Neikter et al. [57] found that texture strength is determined by the grain size of the primary beta phase. Slower cooling, which leads to larger beta phase grains, was shown to result in an increased degree of texture (compared to samples cooled faster—with laser metal wire deposition).

In Fig. 8, the dashed lines indicate the boundaries of the columnar grains parallel to the build direction.

The width of the columnar grains, like their direction, depends on the temperature gradients; the greater the gradient, the smaller the width of the columnar grains. For the alloy studied, it was observed that the width of the columnar grains varied depending on the value of the parameter SF. Figure 9 shows the results of measurements of the columnar grains (primary beta phase columns). The measurements were carried out on a metallographic sample, on a plane perpendicular to the building direction (XY plane). Columnar grains with the highest average width of $\sim 100 \mu\text{m}$ were observed for SF 86, whilst the smallest, with a width of $\sim 70 \mu\text{m}$, were observed for SF 116. For SF 86 and SF 96, the columnar grains were similar in sizes to each other, with differences not exceeding 10%. On the contrary, for SF 116, the columnar grains widths were about 30% smaller than for SF 86. In Fig. 9, the results of the column width measurements were presented. Columnar grain with the largest average width of $110 \mu\text{m}$ were observed for SF 86 top, whilst the smallest, with a width of $61 \mu\text{m}$, were observed for SF 116 bottom. At the bottom part of the sample (bottom), the width of the columnar grain is smaller in the top part of sample.

For a constant cross-section being processed (melted) and for the same process conditions (process temperature), the magnitude of the gradient decreases with the height of the sample [58] the higher the sample, the lower the gradient. It resulted from the fact that the sample produced has a higher thermal conductivity than the powder and also that during the process the volume of

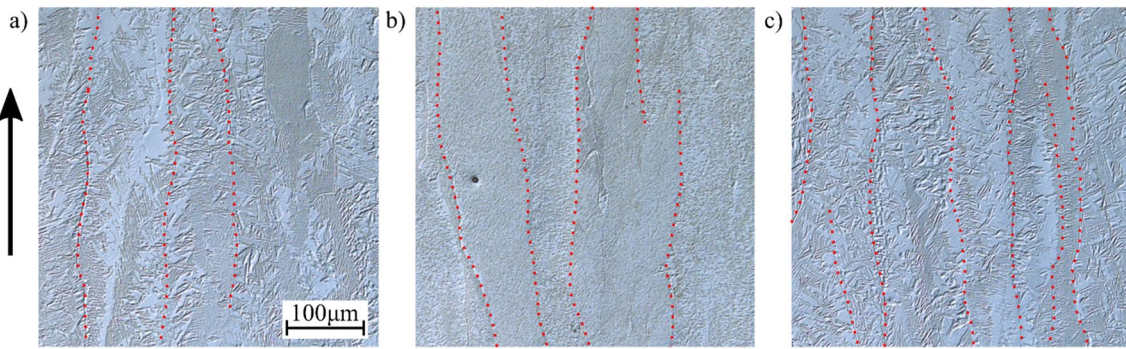


Fig. 8 Comparison of microstructures in relation to SF: **a)** SF 86, **b)** SF 96, and **c)** SF 116; bottom: lines indicate columnar grain boundaries; arrows indicate build direction. Confocal microscope

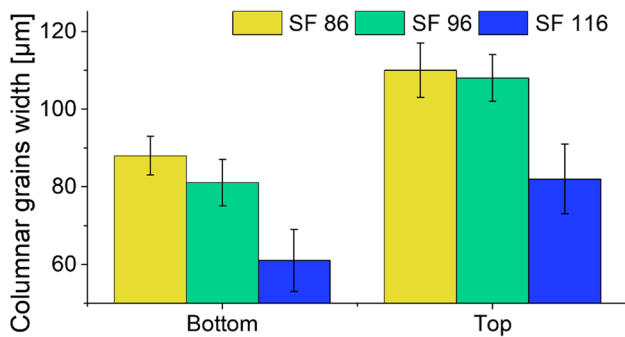


Fig. 9 Comparison of column diameters for different SF values in relation to height, bottom, and top

material allowing thermal energy to accumulate will increase and at the same time the value of the temperature gradient will decrease. The trend of increasing column width with height was maintained for all SF values despite differences in the values of

energy supplied. The average increase in column width between top and bottom, for individual SF values, was around 30%.

Increasing the value of the SF parameter and thus the scanning speed also results in grain refinement [42, 43, 48], and thus, the α -phase plate size decreases, as seen in Fig. 10a–c. The refinement of the α -phase plates with increasing SF parameter is due to the process temperature, which depends on the delivered energy (beam interaction time and beam travel speed). The PBF-EB manufacturing process for SF 86 samples was characterised by a higher process temperature than for SF 116 (Table 2).

Based on the graph shown in Figs. 5 and 7, it can be seen that the site-dependent temperature difference between SF 86 and SF 116 is distinct and is approximately 25°C for the bottom of the sample (bottom) and approximately 27°C for the top of the sample. The noticeable differences in temperature are a direct result of the different energy delivered to the processed samples; for SF 86 it was 34 J mm⁻³, which is about 35% higher than for SF 116 (26 J mm⁻³). Other factors determining fragmentation include the time the material is

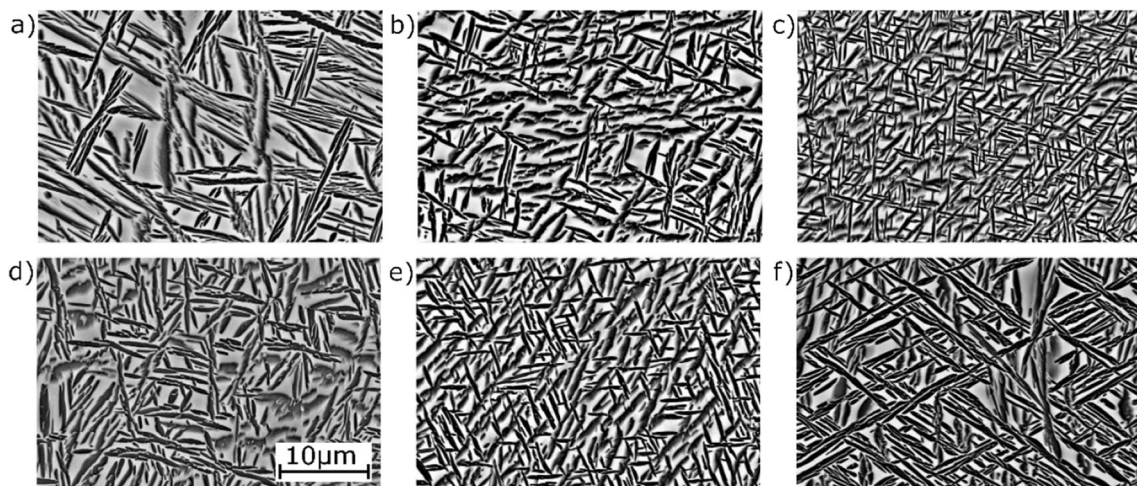
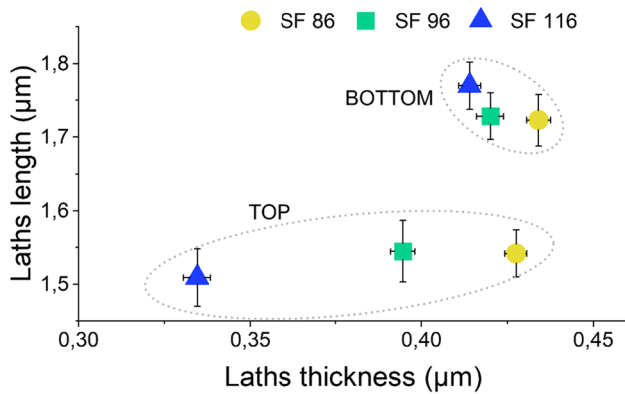


Fig. 10 Microstructure of samples made with different SF. **a)** SF 86_T; **b)** SF 96_T; **c)** SF 116_T; **d)** SF 86_B; **e)** SF 96_B; **f)** SF 116_B; plane XZ; arrow indicates build direction; SEM, BSE

Table 2 Results of porosity (%) measurements for different values of SF

	SF 86	SF 96	SF 116
Top	0.23	0.36	0.37
Bottom	0.19	0.33	0.31
Average	0.21 ± 0.05	0.34 ± 0.02	0.31 ± 0.09

**Fig. 11** Comparison of the thickness and length of α -phase plates in relation to SF

exposed to the beam and the residence time of the samples at a certain temperature. For SF 86, the scanning speed was the lowest of the tested values, and thus, the beam exposure time was the longest. This resulted in the growth of α -phase plates (Fig. 10a). The opposite was true for SF 116, where the high scanning speed resulted in the lowest beam exposure time, reducing the possibility of α -phase plate growth. In our study, the largest α -phase plates were characterised by SF 86 samples (Fig. 10a, d). The differences in grain size for samples made from SF 96 and 116 are not so distinct.

The microstructure analysis also showed differences in the size of α -phase plates depending not only on SF, but also on the height at which the measurement was taken. In the bottom part of the sample, the sizes of the α -phase plates are noticeably larger than for the top part (Fig. 10). The average thickness and length of the α -phase plates in the bottom part of the sample regardless of the SF value were approximately $0.42 \mu\text{m}$ and approximately $1.75 \mu\text{m}$, respectively (Fig. 11). For the top part of the samples, the SF value had an effect on the thickness of the plates, whilst it had a much smaller effect on their length. The highest average lath thickness value was observed for SF 86 ($0.43 \mu\text{m}$, top), the lowest for SF 116 ($0.34 \mu\text{m}$, bottom).

The differences in plate sizes depending on the measurement location (bottom, top) are a direct result of the nature of the PBF-EB process. As it is a hot process, the samples stay at a high temperature for several/several hours. When producing tall specimens, the elevated temperature affected the lower parts of the specimen significantly longer than its upper parts. For the samples tested, the bottom part on average stayed at a

temperature of about $700\text{--}800$ for about 8 h 30min, whilst the top part stayed for less than one hour (about 40 min).

3.4 Porosity

Based on previous studies, it can be concluded that for energies greater than 30 J mm^{-3} it is possible to reduce porosity to values less than 0.1% [46]. Analysis of the process parameters allowed the amount of energy supplied during powder melting to be determined. For SF 86 this was 34 J mm^{-3} , for SF 96, 30 J mm^{-3} whilst for SF 116, 26 J mm^{-3} . Of the three SF values, only for SF 116 was the amount of energy delivered below 30 J mm^{-3} .

For PBF technology, the most common pore types are round pores, lack of fusion, or columnar, chimney pores. Their occurrence depends on a number of factors, beam speed, energy input, scan strategies, etc. [59–61]. In the case of PBF-LB technology, the round shape of the pores may indicate the keyhole phenomenon [62] or that too much energy is supplied and the gas channel is closed during melting [63]. For PBF-EB technology, spherical pores can be the result of porosity in the atomised gas powder [60, 64], from the gas trapped between the powder particles or from the supply of insufficient energy [36, 39] or, more rarely, from the supply of too much energy. Careful analysis of the powder used in all processes showed that the majority of the powder particles did not contain discontinuities (Fig. 12a). Small amount of hollow particles was observed (Fig. 12b). This types of hollow particles may have contributed to the formation of the spherical pores.

Porosity was observed in all samples in the SF range analysed. It ranged from approximately 0.19% (SF 86) to 0.37% (SF 116) (Table 2). Shapes, sizes, and its clustering are presented on Fig. 13. It can be seen that for SF 86 the typical pores are spherical gas pores. For SF 96, there are mainly spherical pores with single, small pores of the lack of fusion type. SF 116 has the same types of pores as SF 86 and SF 96, however, its size and number of pores of the lack of fusion type are larger than those of the other SFs.

On the basis of the analysis of the porosity image of the samples, three types of shapes were distinguished: elongated, subrounded, and round. The roundness parameter (R) described by Eq. (2) was used to describe the shape of the pore,

$$\text{Roundness} = 4 \times \frac{[\text{Area}]}{\pi \times [\text{Major axis}]^2} \quad (2)$$

The group of elongated shapes included all pores for which $R < 0.375$, the subrounded group $0.375 \leq R < 0.675$, and the round group for $R \geq 0.675$. Analysis of the nature and type of porosity of all the samples analysed showed that the main contribution, in terms of both surface area and shape, came from round pores (Table 3).

Fig. 12 Powder particles used in the study, **a)** cross-section of typical particles, **b)** hollow particle with internal gas porosity. SEM, BSE

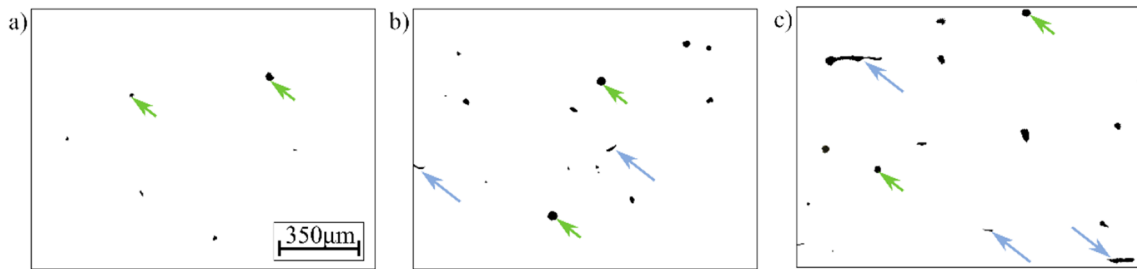
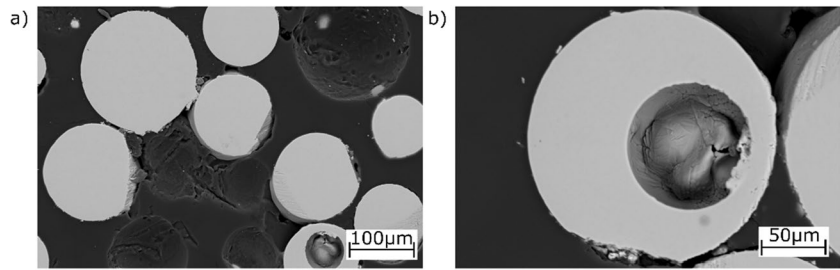


Fig. 13 Examples of shape and distribution of porosity in samples as a function of SF, **a)** SF 86, **b)** SF 96, **c)** SF 116 Arrows indicate pore types; blue (long)—elongated; green (short)—round

Table 3 Comparison of the percentage of pore types and their surface area in relation to SF

Type of pores	SF 86		SF 96		SF 116	
	% of all pores	% of area of all pores	% of all pores	% of area of all pores	% of all pores	% of area of all pores
Elongated	1.6	1.9	4.3	5.8	23.2	34.7
Subrounded	34.4	7.6	34.2	6.8	33.5	9.9
Round	55.7	90.5	61.4	87.4	41.6	55.4

For SF 96 and SF 116, the porosity values are close to each other (Table 3). Analysis of the porosity image of the samples showed that the nature and number of pores were significantly different for these two SF values. For SF 116, 23% of all pores recorded were elongated pores which can be classified as lack of fusion type. For SF 96, this type of pores accounted for only 6%, whilst for SF 86 it was only about 1.5%. In terms of pore area, the share of elongated pores was 34% of the total pore area for SF 116, 5.8% for SF 96, and 1.9% for SF 86. Figure 14 shows the largest example of lack of fusion found on the surface analysed of the SF 116 sample with a length of more than 500 µm.

The appearance of lack of fusion pores is mainly related to insufficient melting of the next layer as a result of insufficient energy supply [26, 65]. Such defects may adversely affect the tensile properties mainly of UTS when located in a plane perpendicular to the loading direction. They also contribute to a reduction in fatigue properties, particularly when located close to the surface [66–68]. These defects are difficult or impossible to remove by hot isostatic pressing,

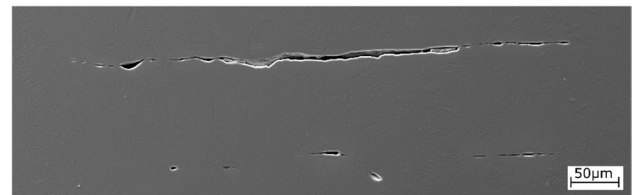


Fig. 14 Lack of fusion with 512 µm length; cross-section of sample SF 116. SEM; SE

depending on their location [68, 69]. Karoluk et al. [70] conducted fatigue tests on PBF-EB-processed Ti-55511 with process parameters similar to use for manufacturing SF 86 samples. Despite relatively low porosity (0.06%) with mainly spherical pores, they observed that the main cause of fatigue cracks in the as-built specimens were lack of fusion defects. These defects acted as the crack initiation site in the as-built specimens. Karoluk et al. in their work also showed that the postprocess HIP treatment effectively eliminated

spherical pores and the effect of lack-of-fusion defects on the fatigue fracture initiations.

3.5 Microhardness

The results of the hardness measurements for samples with different SF values showed that increase in this parameter is not unequivocally related to an increase in hardness (Fig. 15). The highest value was obtained for SF 96 and the lowest for SF 116.

It can also be noted that the confidence intervals are the largest for SF 116 and coincide with the results for the other SF values. Therefore, it can be assumed that, although there are differences in hardness in the lower part, they are not statistically significant. Significant differences occur when comparing the results between the bottom and top parts of the samples; in this case, the differences are on average about 10%, whilst the confidence intervals are much narrower than for the bottom part of the sample.

3.6 Tensile properties

The analysis of the mechanical properties showed that the value of the SF parameter influences the results obtained, but no correlation was observed between the increase in

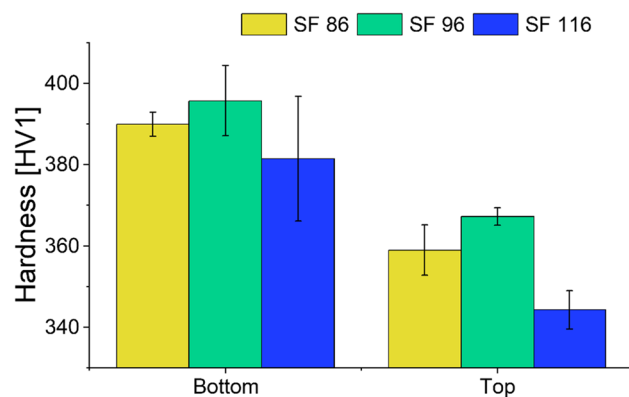
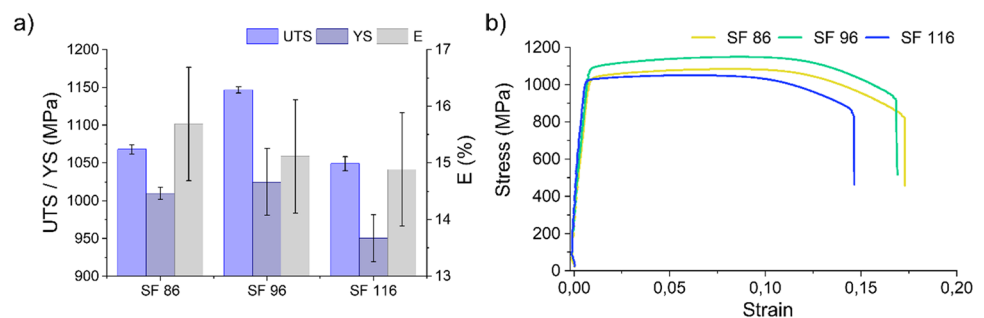


Fig. 15 Comparison of hardness measurements for samples with different SF values

Fig. 16 Comparison of a) mechanical parameters and b) stress–strain characteristics for sample with different SF



mechanical properties and the increase/decrease in the SF parameter.

In Fig. 16a, the results of the UTS, YS, and ϵ measurements are summarised. It can be observed that the highest properties, except for elongation, were recorded for SF 96 samples (UTS 1147 MPa, YS 1025 MPa, ϵ 15.1%), whilst the lowest for SF 116. Figure 16b presents stress–strain characteristics for sample with different SF. Analysing the influence of SF on individual strength parameters, it can be seen that it has the greatest impact on UTS. The difference between the lowest and highest value obtained for the different SF values was approximately 10% (100 MPa), with confidence interval widths of less than 1%. In the case of the yield strength, the difference between the minimum and maximum values was approximately 7%, with the confidence intervals for the individual results being wide enough to overlap (Fig. 16). The situation is similar for elongation; the difference in elongation between the minimum and maximum values is 0.8% with an interval width of 2%. For the parameters YS and ϵ , the impact of SF on the results cannot be clearly determined.

When comparing the properties obtained with the mechanical properties of alloy VT22 described in GOST 26492–85 [71] to manufactured samples, it can be seen that the results are very similar. VT22 in the annealed state has, according to GOST 26492–85, a UTS in the range 1030–1280 MPa with an elongation of 6–10%. This means that the PBF-EB-processed Ti-55511 alloy has mechanical properties similar to the conventionally obtained alloy after heat treatment with BASCA (beta anneal slow cool age). However, it has higher elongation than in the specified standard. Figure 17 shows the tensile fracture of the samples produced with different values of the speed function.

The fractures for samples SF 86 and SF 96 (respectively, Fig. 17a, b) are cup and cone with a clear neck, fibrous zone, and shear lip zone. The fracture in these samples in the first fracture phase (area I) was initiated in the core of the sample (in the plane perpendicular to the manufacturing and tensile axes). In the second phase (area II), the rupture was initiated at the periphery of the neck and a fracture was formed. In both cases (SF 86 and SF 96), there was no influence of material defects on the site of crack initiation and

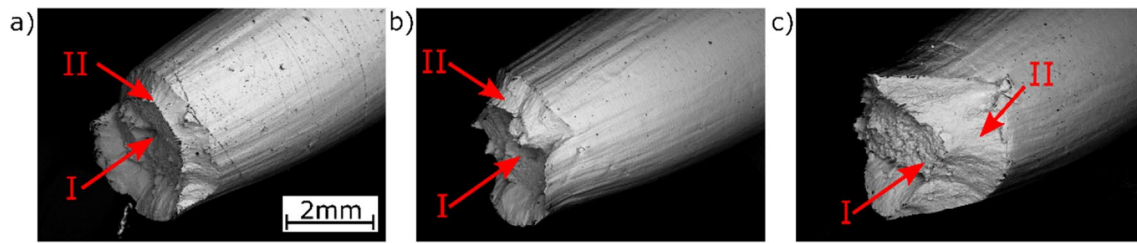


Fig. 17 Comparison of the fracture of 3 samples made with 3 different values of the speed function. **a)** SF 86; **b)** SF 96; **c)** SF 116; I: fibrous zone; II: shear lips

propagation. In the case of the sample produced with SF 116, the fracture (Fig. 17c) looks different from that of SF 86 and SF 96. A constriction is visible, but the fracture itself is asymmetric. The area of the fracture formed in phase I is displaced towards the edge of the sample. In Fig. 18a, it can be observed that the shift in the fracture axis for SF 116 is due to the accumulation of internal defects formed in this area (Fig 18b).

These are mainly defects of the lack-of-fusion type, as well as gas pores and columnar pores. Outside area I, defects of the same type are visible. The lack of fusion can be observed in two places near the edge of the fracture (Fig. 18b). The defects present resulted in a reduction in the active cross section and uneven tension loading, which had a direct impact on the site of crack initiation and propagation. A similar type of fracture was observed for almost all SF 116 samples. This is direct evidence that the type of internal defects and their number influenced the initiation of cracks during axial stretching (relative to the SF 86 and SF 96 samples) and significantly affected the tensile properties.

4 Conclusions

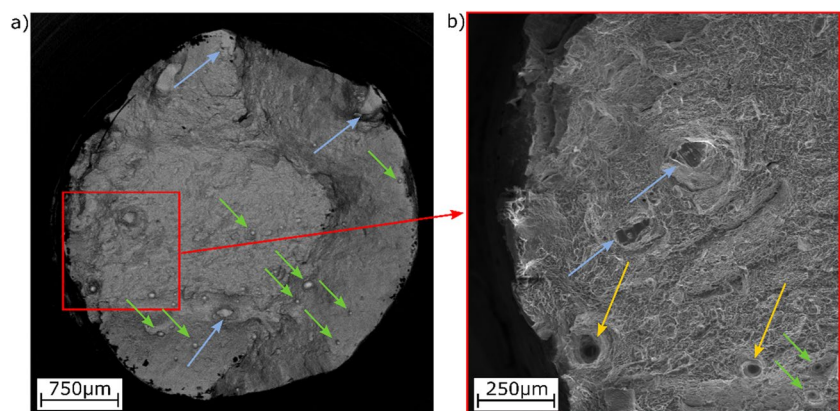
In this work, the influence of SF on the microstructural and mechanical properties of Ti-55511 alloy manufactured by PBF-EB technology was studied. The result show that SF

has a significant effect on the properties of the Ti-55511 alloy: microstructure, phase composition, porosity and strength and limited on microhardness and chemical composition changes. It was also found that SF caused changes in the kinematics of phase transformations in Ti-55511 due to temperature differences in the fabrication process resulting from the delivery of different energy.

The main findings can be summarised as follows:

- The use of different values of the speed function, therefore, higher energy, leads to changes in the temperature of the PBF-EB manufacturing process and to increase the percentage of the β -phase content. Based on the differences in phase content and the calculations performed, increasing the SF from 86 to 116 reduced the process temperature by approximately 50°C.
- The samples made with SF 86 had the largest column diameter of the primary α -phase (110 μm) and were more than 30% larger than those of SF 116 (82 μm). It is also significant that all samples, regardless of series, had a larger column diameter at the top (T) than at the bottom (B) of the samples.
- Increasing the SF in tested samples led to a reduction in the thickness of the resulting α -phase laths (0.33 μm for SF 116 and 0.43 μm for SF 86, respectively). Significant differences in lath thickness were also found between the top and bottom of the SF 116 (0.33 μm top, 0.43 μm

Fig. 18 Fracture area of the sample SF 116, **a)** general view, **b)** area with lack of fusion and different types of pores Arrows indicate defects observed in the fracture: yellow (long) columnar pores, blue (medium) lack of fusion, and green (short) gas pores; SEM



bottom). For other SF differences were smaller, less than 0.05 μm , and SF 96.

- In all samples analysed, the porosity did not exceed 0.34% (SF 96). However, SF influenced their shape, increasing SF resulted in change of the dominant type of pores from round (SF 86) to elongated (SF 116).
- Increase in SF from 86 to 96 resulted in increase of UTS and YS as a direct result of the finer microstructure. However, although the SF 116 samples were characterised by even finer lamellae, the amount of elongated pores resulted in a final reduction in the strength of samples in this series.

Author contribution All persons who meet authorship criteria are listed as authors, and all authors certify that they have participated sufficiently in the work to take public responsibility for the content, including participation in the concept, design, analysis, writing, or revision of the manuscript. Marcin Madeja: conceptualization, methodology, data curation, investigation, visualisation, writing—original draft, and writing—review and editing. Robert Dziedzic: methodology, investigation, formal analysis, validation, writing—review and editing.

Funding This work was supported by the Polish National Centre for Research and Development within the project: INNOLOT/I/6/NCBR/2013–AMpHOra “Research on Additive Manufacturing Processes and Hybrid Operations for Development of Innovative Aircraft Technology.”

Data availability Representative samples of the research data are given in the figures. Other datasets generated and/or analysed during this study are not publicly available due to their large size but are available from the corresponding author on reasonable request.

Declarations

Competing interests The authors declare no competing interests.

Open Access This article is licensed under a Creative Commons Attribution 4.0 International License, which permits use, sharing, adaptation, distribution and reproduction in any medium or format, as long as you give appropriate credit to the original author(s) and the source, provide a link to the Creative Commons licence, and indicate if changes were made. The images or other third party material in this article are included in the article's Creative Commons licence, unless indicated otherwise in a credit line to the material. If material is not included in the article's Creative Commons licence and your intended use is not permitted by statutory regulation or exceeds the permitted use, you will need to obtain permission directly from the copyright holder. To view a copy of this licence, visit <http://creativecommons.org/licenses/by/4.0/>.

References

- Liu X, Chu P, Ding C (2004) Surface modification of titanium, titanium alloys, and related materials for biomedical applications. *Mater Sci Eng: R: Rep* 47(3–4):49–121. ISSN 0927-796X. <https://doi.org/10.1016/j.mser.2004.11.001>
- Peters M, Kumpfert J, Ward CH, Leyens C (2003) Titanium alloys for aerospace applications. *Adv Eng Mater* 5:419–427. <https://doi.org/10.1002/adem.200310095>
- Ezugwu EO, Wang ZM (1997) Titanium alloys and their machinability—a review. *J Mater Process Technol* 68(3):262–274. [https://doi.org/10.1016/S0924-0136\(96\)00030-1](https://doi.org/10.1016/S0924-0136(96)00030-1)
- Zhang L-C, Chen L-Y (2019) A review on biomedical titanium alloys: recent progress and prospect. *Adv Eng Mater* 21:1801215. <https://doi.org/10.1002/adem.201801215>
- Zhang Z, Li Z, Pan S, Chai X (2022) Enhanced strength and high-temperature wear resistance of Ti6Al4V alloy fabricated by laser solid forming. *ASME. J Manuf Sci Eng* 144(11):111011. <https://doi.org/10.1115/1.4054901>
- Tardelli J, Bolfarini C, Reis A (2020) Comparative analysis of corrosion resistance between beta titanium and Ti-6Al-4V alloys: a systematic review. *J Trace Elem Med Biol* 62:126618. <https://doi.org/10.1016/j.jtemb.2020.126618>
- Schiff N, Grosgeat B, Lissac M, Dalard F (2002) Influence of fluoride content and pH on the corrosion resistance of titanium and its alloys. *Biomaterials* 23(9):1995–2002. [https://doi.org/10.1016/S0142-9612\(01\)00328-3](https://doi.org/10.1016/S0142-9612(01)00328-3)
- de Assis SL, Wolyneć S, Costa I (2006) Corrosion characterization of titanium alloys by electrochemical techniques. *Electrochimica Acta* 51(8–9):1815–1819. <https://doi.org/10.1016/j.electacta.2005.02.121>
- Chen B, Xiong F, Tang H, He L, Hu S (2020) Effect of cooling method on small diameter blind-hole drilling of new β -type dental Ti-Zr-Nb alloy. *J Manuf Process* 59:421–431. <https://doi.org/10.1016/j.jmapro.2020.10.013>
- Li CC, Xin C, Wang Q, Ren JQ, Zhao B, Wu JP, Pan XL, Lu XF (2023) A novel low-cost high-strength β titanium alloy: microstructure evolution and mechanical behavior. *J Alloys Compd* 959:170497. <https://doi.org/10.1016/j.jallcom.2023.170497>
- Zhao Q et al (2022) High-strength titanium alloys for aerospace engineering applications: a review on melting-forging process. *Mater Sci Eng A* 845:143260. <https://doi.org/10.1016/j.msea.2022.143260>
- Ivasyshyn IM, Markovskiy PE, Havrysh IM, Karasevskaya IP (2014) Influence of cooling rate in the process of hardening on the aging and formation of the mechanical Characteristics of VT22 Titanium Alloy. *Mater Sci* 50:62–69. <https://doi.org/10.1007/s11003-014-9692-9>
- Warlimont H (2018) Titanium and titanium alloys. In: Warlimont H, Martienssen W (eds) Springer handbook of materials data. Springer handbooks. Springer, Cham. https://doi.org/10.1007/978-3-319-69743-7_7
- Zhang J, Cheng X, Li Z (2010) Total fatigue life prediction for Ti-alloys airframe structure based on durability and damage-tolerant design concept. *Mater Des* 31:4329–4335. <https://doi.org/10.1016/j.matdes.2010.03.052>
- Ratochka IV, Mishin IP, Lykova ON et al (2016) Structural evolution and mechanical properties of a VT22 titanium alloy under high-temperature deformation. *Russ Phys J* 59:397–402. <https://doi.org/10.1007/s11182-016-0786-8>
- Łukaszewicz A, Szota M (2017) Influence of production method on selected properties of VT 22 titanium alloy. *Arch Mater Sci Eng* 87:27–32. <https://doi.org/10.5604/01.3001.0010.5968>
- Madeja M, Karoluk M, Smolina I (2020) Welding of Ti-5Al-5Mo-5 V-1Cr-1Fe parts manufactured in the Electron Beam Melting. *Mater Des* 195:108969. <https://doi.org/10.1016/j.matdes.2020.108969>
- Moiseyev VN (2005) Titanium alloys: Russian Aircraft and Aerospace Applications (1st ed). CRC Press. <https://doi.org/10.1201/9781420037678>
- Froes FH, Bomberger HB (1985) The beta titanium alloys. *JOM* 37:28–37. <https://doi.org/10.1007/BF03259693>

20. Jones NG, Dashwood RJ, Dye D, Jackson M (2008) Thermo-mechanical processing of Ti-5Al-5Mo-5V-3Cr. *Mater Sci Eng: A* 490:369–377. <https://doi.org/10.1016/j.msea.2008.01.055>
21. Weiss I, Semiatin SL (1998) Thermomechanical processing of beta titanium alloys: an overview. *Mater Sci Eng: A* 243:46–65. [https://doi.org/10.1016/S0921-5093\(97\)00783-1](https://doi.org/10.1016/S0921-5093(97)00783-1)
22. Lütjering G (1998) Influence of processing on microstructure and mechanical properties of (α + β) titanium alloys. *Mater Sci Eng: A* 243:32–45. [https://doi.org/10.1016/S0921-5093\(97\)00778-8](https://doi.org/10.1016/S0921-5093(97)00778-8)
23. Ivasishin OM, Markovsky PE, Semiatin SL, Ward CH (2005) Aging response of coarse- and fine-grained β titanium alloys. *Mater Sci Eng: A* 405:196–305. <https://doi.org/10.1016/j.msea.2005.06.027>
24. Salmi A, Calignano F, Galati M, Atzeni E (2018) An integrated design methodology for components produced by laser powder bed fusion (L-PBF) process. *Virtual Phys Prototyp* 13:191–202. <https://doi.org/10.1080/17452759.2018.1442229>
25. Ford S, Despeisse M (2016) Additive manufacturing and sustainability: an exploratory study of the advantages and challenges. *J Clean Prod* 137:1573–1587. <https://doi.org/10.1016/j.jclepro.2016.04.150>
26. Herzog D, Seyda V, Wycisk E, Emmelmann C (2016) Additive manufacturing of metals. *Acta Mater* 117:371–392. <https://doi.org/10.1016/j.actamat.2016.07.019>
27. Schwab H, Palm F, Kühn U, Eckert J (2016) Microstructure and mechanical properties of the near-beta titanium alloy Ti-5553 processed by selective laser melting. *Mater Des* 105:75–80. <https://doi.org/10.1016/j.matdes.2016.04.103>
28. Guo C, Ge W, Lin F (2015) Effects of scanning parameters on material deposition during electron beam selective melting of Ti-6Al-4V powder. *J Mater Process Technol* 217:148–157. <https://doi.org/10.1016/j.jmatprotec.2014.11.010>
29. Chen Y, Yue H, Wang X (2018) Microstructure, texture and tensile property as a function of scanning speed of Ti-47Al-2Cr-2Nb alloy fabricated by selective electron beam melting. *Mater Sci Eng A* 713:195–205. <https://doi.org/10.1016/j.msea.2017.12.020>
30. Wu K, Ma S, Fang X et al (2023) Microstructure and mechanical properties of an in-situ TiB₂ particle reinforced AlSi10Mg composite additive manufactured by selective electron beam melting. *J Mater Sci* 58:7915–7929. <https://doi.org/10.1007/s10853-023-08516-1>
31. Wang L, Zhang YM, Chia HY, Yan WT (2022) Mechanism of keyhole pore formation in metal additive manufacturing. *NPJ Comput Mater* 27:1–11. <https://doi.org/10.1038/s41524-022-00699-6>
32. Zhao C et al (2020) Critical instability at moving keyhole tip generates porosity in laser melting. *Science* 370:1080–1086. <https://doi.org/10.1126/science.abd1587>
33. Wang L, Zhang Y, Yan W (2020) Evaporation model for keyhole dynamics during additive manufacturing of metal. *Phys Rev Appl* 14:064039. <https://doi.org/10.1103/PhysRevApplied.14.064039>
34. Fox JC (2018) Transient melt pool response in additive manufacturing of Ti-6Al-4V. Carnegie Mellon University. Thesis. <https://doi.org/10.1184/R1/6724049.v1>
35. Barbagallo R, Di Bella S, Mirone G, La Rosa G (2022) Study of the electron beam melting process parameters' influence on the tensile behavior of 3D printed Ti6Al4V ELI alloy in static and dynamic conditions. *Materials* 15:4217. <https://doi.org/10.3390/ma15124217>
36. Cunningham R, Narra SP, Ozturk T et al (2016) Evaluating the effect of processing parameters on porosity in electron beam melted Ti-6Al-4V via synchrotron X-ray microtomography. *JOM* 68:765–771. <https://doi.org/10.1007/s11837-015-1802-0>
37. Gong X, Lydon J, Cooper K, Chou K (2014) Beam speed effects on Ti-6Al-4V microstructures in electron beam additive manufacturing. *J Mater Res* 29:1951–1959. <https://doi.org/10.1557/jmr.2014.125>
38. Silvestri AT, Foglia S, Borrelli R, Franchitti S, Pirozzi C, Astarita A (2020) Electron beam melting of Ti6Al4V: role of the process parameters under the same energy density. *J Manuf Process* 60:162–179. <https://doi.org/10.1016/j.jmapro.2020.10.065>
39. Gong H, Rafi K, Gu H et al (2014) Analysis of defect generation in Ti-6Al-4V parts made using powder bed fusion additive manufacturing processes. *Addit Manuf* 1:87–98. <https://doi.org/10.1016/j.addma.2014.08.002>
40. Unocic KA, Kirka MM, Cakmak E et al (2020) Evaluation of additive electron beam melting of haynes 282 alloy. *Mater Sci Eng A* 772:138607. <https://doi.org/10.1016/j.msea.2019.138607>
41. Cheng B, Price S, Gong X et al (2014) Speed function effects in electron beam additive manufacturing. *ASME Int Mech Eng Congr Expo Proc* 2A:1–9. <https://doi.org/10.1115/IMECE2014-36664>
42. Morita T, Tsuda C, Nakano T (2017) Influences of scanning speed and short-time heat treatment on fundamental properties of Ti-6Al-4V alloy produced by EBM method. *Mater Sci Eng A* 704:246–251. <https://doi.org/10.1016/j.msea.2017.08.020>
43. Wang X, Chou K (2018) EBSD study of beam speed effects on Ti-6Al-4V alloy by powder bed electron beam additive manufacturing. *J Alloys Compd* 748:236–244. <https://doi.org/10.1016/j.jallcom.2018.03.173>
44. Wang X, Gong X, Chou K (2015) Scanning speed effect on mechanical properties of Ti-6Al-4V alloy processed by electron beam additive manufacturing. *Procedia Manuf* 1:287–295. <https://doi.org/10.1016/j.promfg.2015.09.026>
45. Wang C, Tan X, Liu E, Tor SB (2018) Process parameter optimization and mechanical properties for additively manufactured stainless steel 316L parts by selective electron beam melting. *Mater Des* 147:157–166. <https://doi.org/10.1016/j.matdes.2018.03.035>
46. Kurzynowski T, Madeja M, Dziedzic R, Kobiela K (2019) The effect of EBM process parameters on porosity and microstructure of Ti-5Al-5Mo-5V-1Cr-1Fe alloy. *Scanning* 2019. <https://doi.org/10.1155/2019/2903920>
47. Committee of Standardization and Metrology of the USSR. Wrought titanium and titanium alloys. Grades, Gost 19807-91
48. Körner C (2016) Additive manufacturing of metallic components by selective electron beam melting - a review. *Int Mater Rev* 61:361–377. <https://doi.org/10.1080/09506608.2016.1176289>
49. De Formanoir C, Michotte S, Rigo O, Germain L (2016) Materials Science & Engineering A Electron beam melted Ti - 6Al - 4V : microstructure, texture and mechanical behavior of the as-built and heat-treated material. *Mater Sci Eng A* 652:105–119. <https://doi.org/10.1016/j.msea.2015.11.052>
50. Sames W (2015) Additive manufacturing of inconel 718 using electron beam melting: Processing, Post-Processing, & Mechanical Properties. Doctoral dissertation, Texas A & M University. <https://hdl.handle.net/1969.1/155230>
51. Rodgers TM, Lim H, Brown JA (2020) Three-dimensional additively manufactured microstructures and their mechanical properties. *JOM* 72:75–82. <https://doi.org/10.1007/s11837-019-03808-x>
52. Priya P, Mercer B, Huang S et al (2020) Towards prediction of microstructure during laser based additive manufacturing process of Co-Cr-Mo powder beds. *Mater Des* 196:109117. <https://doi.org/10.1016/j.matdes.2020.109117>
53. Al-Bermani SS, Blackmore ML, Zhang W, Todd I (2010) The origin of microstructural diversity, texture, and mechanical properties in electron beam melted Ti-6Al-4V. *Metall Mater Trans A Phys Metall Mater Sci* 41:3422–3434. <https://doi.org/10.1007/s11661-010-0397-x>
54. Paul S, Liu J, Strayer ST et al (2020) A discrete dendrite dynamics model for epitaxial columnar grain growth in metal additive manufacturing with application to Inconel. *Addit Manuf* 36:101611. <https://doi.org/10.1016/j.addma.2020.101611>

55. Basak A, Das S (2016) Epitaxy and microstructure evolution in metal additive manufacturing. *Annu Rev Mater Res* 46:125–149. <https://doi.org/10.1146/annurev-matsci-070115-031728>
56. Formanoir C, Michotte S, Rigo O, Germain L, Godet S (2016) Electron beam melted Ti–6Al–4V: microstructure, texture and mechanical behavior of the as-built and heat-treated material. *Mater Sci Eng, A* 652:105–119. <https://doi.org/10.1016/j.msea.2015.11.052>
57. Neikter M, Woracek R, Durniak C, Persson M et al (2020) Texture of electron beam melted Ti-6Al-4V measured with neutron diffraction. *MATEC Web Conf* 321:03021. <https://doi.org/10.1051/mateconf/202032103021>
58. Tan X, Kok Y, Tan YJ et al (2015) Graded microstructure and mechanical properties of additive manufactured Ti-6Al-4V via electron beam melting. *Acta Mater* 97:1–16. <https://doi.org/10.1016/j.actamat.2015.06.036>
59. Cordero ZC, Dinwiddie RB, Immel D, Dehoff RR (2017) Nucleation and growth of chimney pores during electron-beam additive manufacturing. *J Mater Sci* 52:3429–3435. <https://doi.org/10.1007/s10853-016-0631-z>
60. Bauereiß A, Scharowsky T, Körner C (2014) Defect generation and propagation mechanism during additive manufacturing by selective beam melting. *J Mater Process Technol* 214:2522–2528. <https://doi.org/10.1016/j.jmatprotec.2014.05.002>
61. Tammam-Williams S, Zhao H, Léonard F et al (2015) XCT analysis of the influence of melt strategies on defect population in Ti-6Al-4V components manufactured by Selective Electron Beam Melting. *Mater Charact* 102:47–61. <https://doi.org/10.1016/j.matchar.2015.02.008>
62. Ge W, Fuh JYH, Na SJ (2021) Numerical modelling of keyhole formation in selective laser melting of Ti6Al4V. *J Manuf Process* 62:646–654. <https://doi.org/10.1016/j.jmapro.2021.01.005>
63. Gong H, Rafi K, Gu H et al (2015) Influence of defects on mechanical properties of Ti-6Al-4V components produced by selective laser melting and electron beam melting. *Mater Des* 86:545–554. <https://doi.org/10.1016/j.matdes.2015.07.147>
64. Ackelid U, Svensson M (2009) Additive manufacturing of dense metal parts by electron beam melting Materials science and technology conference. MS&T Partner Societies, Pittsburgh, pp 2711–2719. 2719
65. Zhai Y, Galarraga H, Lados DA (2016) Microstructure, static properties, and fatigue crack growth mechanisms in Ti-6Al-4V fabricated by additive manufacturing: LENS and EBM. *Eng Fail Anal* 69:3–14. <https://doi.org/10.1016/j.engfailanal.2016.05.036>
66. Tammam-Williams S, Withers PJ, Todd I, Prangnell PB (2017) The influence of porosity on fatigue crack initiation in additively manufactured titanium components. *Sci Rep* 7:1–13. <https://doi.org/10.1038/s41598-017-06504-5>
67. Günther J, Tröster T, Weidner A, Leuders S (2017) Fatigue behavior of Ti-6Al-4V additively manufactured by selective laser and electron beam melting – on the impact of the chemical composition, process-induced porosity and surface roughness. *Dtsch Verband Mater Prüfung e.V.* 89–98
68. du Plessis A, Macdonald E (2020) Hot isostatic pressing in metal additive manufacturing: X-ray tomography reveals details of pore closure. *Addit Manuf* 34:101191. <https://doi.org/10.1016/j.addma.2020.101191>
69. Li P, Warner DH, Pegues JW et al (2019) Investigation of the mechanisms by which hot isostatic pressing improves the fatigue performance of powder bed fused Ti-6Al-4V. *Int J Fatigue* 120:342–352. <https://doi.org/10.1016/j.ijfatigue.2018.10.015>
70. Karoluk M, Kobiela K, Madeja M, Dziedzic R, Ziółkowski G, Kurzynowski T (2023) The effect of postprocessing on the fatigue properties of Ti-5Al-5Mo-5V-1Cr-1Fe produced using electron beam melting. *Materials* 16:1201. <https://doi.org/10.3390/ma16031201>
71. GOST 26492-85 The rolled bars for titanium and titanium alloys. Specification
72. Galati M, Iuliano L (2018) A literature review of powder-based electron beam melting focusing on numerical simulations. *Addit Manuf* 19:1–20. <https://doi.org/10.1016/j.addma.2017.11.001>
73. Wan HL, Wang QZ, Lin HX (2016) The effect of lack-of-fusion porosity on fatigue behavior of additive manufactured titanium alloy. *KEM*. <https://doi.org/10.4028/www.scientific.net/kem.723.44>

Publisher's Note Springer Nature remains neutral with regard to jurisdictional claims in published maps and institutional affiliations.